Output from a Josephson stimulated terahertz amplified radiation emitter

Richard A. Klemm[1,*] and Kazuo Kadowaki[2,†]

[1]*Department of Physics, University of Central Florida, Orlando, FL 32816, USA*

[2]*Graduate School of Pure & Applied Sciences, University of Tsukuba, 1-1-1, Tennodai, Tsukuba, Ibaraki 305-8573, Japan*

(Dated: July 28, 2010)

Abstract

The angular dependence of the radiation-zone output power and electric polarization of stimulated terahertz amplified radiation (STAR) emitted from a *dc* voltage applied across cylindrical and rectangular stacks of intrinsic Josephson junctions is calculated. The boundary conditions are obtained from Love's equivalence principles. During coherent emission, a spatially uniform *ac* Josephson current density in the stack acts as a surface electric current density antenna source, leading to an harmonic radiation frequency spectrum, as in experiment, but absent in all cavity models of cylindrical mesas. Spatial fluctuations of the *ac* Josephson current allow its fundamental mode to lock onto the lowest finite energy cylindrical cavity mode, causing it to resonate, leading to a non-uniform magnetic surface current density radiation source, and a non-trivial combined fundamental frequency output power with linear polarization for general radiation directions, which may be fully or partially coherent. The higher *ac* Josephson harmonics do not excite other cylindrical cavity modes. For rectangular mesas, the lowest energy modes are empirically not excited, but the non-uniform *ac* Josephson current can excite the harmonic sequence of modes with spatial variation across the rectangular widths, leading to combined radiation outputs both for the fundamental and the higher harmonics, which combinations also may be either fully or partially coherent. The superconducting substrate is modeled as a perfect magnetic conductor, greatly reducing the STAR emitter power and modifying its angular dependence, especially parallel to the substrate. Based upon this substrate model, existing $Bi_2Sr_2CaCu_2O_{8+\delta}$ crystals atop perfect electric conductors could have STAR emitter power in excess of 5 mW, acceptable for many device applications.

PACS numbers: 07.57.Hm, 74.50.+r, 85.25.Cp

I. INTRODUCTION

The recent discovery of coherent THz radiation emitted from mesas of the high-temperature superconductor $Bi_2Sr_2CaCu_2O_{8+\delta}$ (BSCCO) has caused a great deal of excitement[1, 2]. In these experiments, rectangular mesas were fashioned by Ar ion milling of a single crystal of BSCCO, with a Au layer covering the mesa's top, to which an electrical lead was attached, and two additional electrical leads were attached to the remaining BSCCO crystal substrate. Typical rectangular mesa dimensions were $60 \times 300 \times 1\ \mu$m. By applying a static (dc) voltage V_0 across the mesa, the ac Josephson effect was generated in each of the $N \sim 10^3$ junctions involved in the mesa, and coherent ac Josephson radiation at THz frequencies was emitted. The ac Josephson relation is

$$\omega_J = \frac{2eV_0}{\hbar N}, \tag{1}$$

where $2e$ is the magnitude of the Cooper pair charge and $\hbar$ is Planck's constant divided by 2π. Equation (1) relates the ac Josephson frequency $\nu_J = \omega_J/(2\pi)$ to the applied V_0/N. To avoid confusion, here we write $\boldsymbol{k}$ and $\boldsymbol{x}$ for the wave vectors and positions outside the mesa, and $\boldsymbol{k}'$ and $\boldsymbol{x}'$ for the wave vectors and positions inside the mesa. Since the frequencies are the same inside and outside the mesa, they are left unprimed.

A. Rectangular mesas

Since BSCCO is a stack of Josephson junctions, with atomically thin superconducting layers separated by thicker dielectric layers, it is extremely anisotropic. In analogy with standard antenna theory[3–5], to zeroth order, one might consider a BSCCO mesa to be a dielectric sandwiched between two metallic layers, as first suggested in the pioneering work of Bulaevskii and Koshelev[6, 7], forming a cavity that produces the electric field which generates the radiation[6–20]. In this cavity model, it was usually assumed that the ac component of the electric field $\boldsymbol{E}(\boldsymbol{x}', t)$ and the ac Josephson supercurrent $\boldsymbol{J}(\boldsymbol{x}', t)$ both had antisymmetric spatial configurations, with maxima along the length ℓ edges, and a node in the center of the mesas of width w, leading to a radiation fundamental wavelength $\lambda = 2w$. The wave vectors of very thin (with height $h \ll \ell, w$) rectangular cavity modes are

$$k'_{mp} = \pi\Big[\Big(\frac{m}{w}\Big)^2 + \Big(\frac{p}{\ell}\Big)^2\Big]^{1/2}, \tag{2}$$

where m and p are integers, when there is no spatial variation of the electromagnetic fields in the $\hat{\boldsymbol{z}}$ direction normal to the layers. These modes are generated from the boundary conditions, which allow for half-integral multiples of wavelengths across the width and the length of the cavity. Usually, such modes in a cavity that is open on the sides only arise when the tangential component $H_{||}$ of the *ac* magnetic field $\boldsymbol{H}(\boldsymbol{x}', t)$ vanishes at the edge of the cavity, unlike previous assumptions[6–20], forcing the normal derivative of $\boldsymbol{E}(\boldsymbol{x}', t)$ to vanish there. Inside the mesa, electromagnetic waves propagate parallel to the layers according to the dispersion relation

$$\omega_{mp} \;=\; \frac{ck'_{mp}}{n_r}, \tag{3}$$

where $n_r \approx \sqrt{\epsilon}$ is the index of refraction, and $\epsilon \approx 18$ for BSCCO in the relevant frequency range[1, 2]. By varying the *dc* V_0 experimentally, radiation is found to occur after one of the harmonic *ac* Josephson frequencies $n\nu_J$ locks onto that of a particular $(m_0 p_0)$ rectangular cavity mode,

$$n\omega_J \;=\; \omega_{m_0 p_0} = \frac{ck'_{m_0 p_0}}{n_r}. \tag{4}$$

In experiments on rectangular samples, it appears that the fundamental $n = 1$ *ac* Josephson frequency ν_J locks onto the rectangular cavity (10) mode frequency, so that $\nu_J = c/(2n_r w)$, also allowing for the higher *ac* Josephson harmonics with $n > 1$ to lock onto the higher cavity $(m0)$ modes, where $m = n$. The temperature T dependence of the radiation power is very unusual, as it vanishes both at low T and at some $T \leq T_c$, with a maximum that can be either broad or sharp, depending upon the sample [2]. In addition, experiments on the angular dependence of the radiation from rectangular mesas of BSCCO have concluded that the radiation from the *ac* Josephson current source is of comparable strength to the radiation from the excited electromagnetic cavity mode [21].

One might wonder why the low energy excitations were not along the length of the rectangular mesa, rather than along the width, as observed experimentally. Although the experiments on rectangular mesas provided evidence for radiation frequencies $\nu_{m0} \propto m/w$ up to four harmonics of ν_J[1, 2], a lower set of modes with harmonic frequencies would be $\nu_{0p} \propto p/\ell$, especially for $w \ll \ell$. Recent experiments suggested that standing waves along the lengths of rectangular mesas might occur[22], although it is presently uncertain whether these modes radiate. A possible resolution of this apparent paradox was suggested

to arise from the component of $\boldsymbol{H}(\boldsymbol{x}', t)$ normal to the mesa side containing the rectangular length, which was predicted to have a half-wavelength spatial variation across the rectangular width[18].

However, this cavity analogy neglects the radiation from the real *ac* Josephson supercurrent $\boldsymbol{J}(\boldsymbol{x}', t)$ across each of the junctions. Therefore, the second zeroth order model is to treat the mesa as a conducting dipole antenna with an *ac* current source, as commonly used in microwave relay stations[3, 4, 15, 16, 18, 23]. In this picture, the most important part of the *ac* Josephson current is its uniform portion across the mesa. This portion leads to a non-vanishing $\boldsymbol{H}(\boldsymbol{x}', t)$ within the mesa arising from Ampère's law. The important question then, is how to treat the Ampère boundary condition. This has been done in very different ways, with inconsistent results.

B. The Ampère boundary condition

Bulaevskii and Koshelev studied the damped Lawrence-Doniach equations for the intrinsic Josephson junctions in thick, long rectangular mesas (with $\ell > h > w$, unlike the case considered here), and concluded that the magnetic induction $\boldsymbol{B}$ should be parallel to each edge, with $\boldsymbol{E}||\hat{\boldsymbol{z}}$, normal to the substrate[6, 7]. In their pioneering treatment of the boundary conditions, they obtained $|\boldsymbol{B}/\boldsymbol{E}| = \pm\zeta_\omega(k_z)$ at the sample surface, where $\zeta_\omega(k_z) = |k_\omega|(k_\omega^2 - k_z^2)^{-1/2}$ for $|k_z| < 2\pi\nu_J/c = k_\omega$, and $\zeta_\omega(k_z) = -ik_z(k_z^2 - k_\omega^2)^{-1/2}$ for $k_z > k_\omega$. In the uniform ($k_z \to 0$) limit, $\zeta_\omega \to 1$. The same sort of model for the boundary conditions was studied with $\zeta_\omega = Z(\omega)$, a complex constant, by Lin and Hu[9–11], a frequency-independent constant by Lin, Hu, and Tachiki[17], and $\zeta_\omega = \gamma = 0.1$ by Tachiki *et al.*[18]. Hu and Lin set the tangential component of $\boldsymbol{B} = 0$ on the edge of cylindrical mesas, but did not take account of the *ac* Josephson current in the Ampère boundary condition[13, 14]. Matsumoto *et al.* treated the Ampère boundary condition as providing constraints on $\boldsymbol{B}$ on opposite sides of the long rectangular mesas in their numerical studies[15, 16]. Koyama *et al.* treated the *ac* Josephson current as uniform in the mesa[20]. The general problem with these models for the boundary conditions is that the approximations used to obtain either γ or $\zeta_\omega(k_z)$ limited the applicability of the expressions, and subsequent workers made different choices for those quantities. In the radiation zone, one expects $\zeta_\omega = \gamma = \pm 1$, but at the edge of the sample, $\boldsymbol{B}$ is subject to the Ampère boundary condition, which depends upon the *ac*

Josephson current within the mesa.

Knowledge of the boundary conditions can lead to a determination of the electromagnetic fields in the near field adjacent to the source. However, in order to obtain the far-field radiation measured in experiment, it is first necessary to construct effective current sources from those boundary conditions, and then to integrate over the current sources weighted with the outgoing wave form [3, 4]. The main point of the present work is that all of the previous treatments of the boundary conditions did not include the possibility of the uniform part of the *ac* Josephson current, or equivalently, the magnetic field generated by the uniform *ac* Josephson current, as an additional radiation source, but instead focussed upon on the electric field as the sole radiation source. If the amplification of the radiation from the excitation of an electromagnetic cavity mode by the inhomogeneous part of the *ac* Josephson current were sufficiently strong, then one could indeed neglect the magnetic field as a radiation source, as was done in the above treatments. However, experiments on the angular dependence of the radiation from rectangular mesas of BSCCO have concluded that the radiation from the electric dipole source equivalent to the neglected magnetic field source is of comparable strength to the radiation from the excited electromagnetic cavity mode [21]. Hence, the boundary conditions should be reexamined.

Here we study the simplest and least ambiguous way to treat this boundary condition. We use Love's equivalence principles[3, 4, 24, 25], which are variations on Huygens' principle, treating the mesa as both electric conductor and magnetic conductor radiation sources[3, 4, 25]. That is, $\boldsymbol{E}(\boldsymbol{x}', t)$ within the mesa is replaced by a surface magnetic current density source $\boldsymbol{M}_S(\boldsymbol{x}', t) = -\hat{\boldsymbol{n}} \times \boldsymbol{E}(\boldsymbol{x}', t)|_S$ by the Love electric conductor equivalence principle, and $\boldsymbol{H}(\boldsymbol{x}', t)$ inside the mesa is replaced by a surface electric current density source $\boldsymbol{J}_S(\boldsymbol{x}', t) = \hat{\boldsymbol{n}} \times \boldsymbol{H}(\boldsymbol{x}', t)|_S$, using the Love magnetic conductor equivalence principle[3, 4, 25]. We emphasize that the situation under study involves both a *real, nonlinear ac* Josephson current that generates electromagnetic waves at multiple harmonic frequencies and a *linear* electromagnetic cavity that obeys Maxwell's equations, which fixes the harmonic frequencies present in the *ac* Josephson current to the appropriate cavity dimension, and depending upon the geometry, can amplify one or more of those harmonics. Thus, unlike other radiation sources studied to date, the THz radiation from BSCCO mesas can only be understood completely by this dual-source mechanism. A sketch of a cylindrical mesa with a uniform $\boldsymbol{J}_S$ and a nonuniform $\boldsymbol{M}_S$ corresponding to the (11) cylindrical cavity mode is shown in

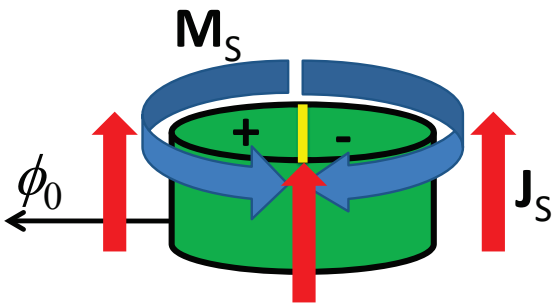

FIG. 1: (Color online) Sketch of a cylindrical mesa with a surface electric current density $\boldsymbol{J}_S$ (red vertical arrows) and a magnetic current density $\boldsymbol{M}_S$ (blue horizontal azimuthal arrows). The $\pm$ signs refer to the signs of the (11) cavity mode, separated by the yellow line, with fixed angle ϕ_0 indicated by the thin horizontal black arrow.

Fig. 1. This combination of equivalence principles allows us to obtain analytic forms for the distinct angle dependence, polarization, and frequency dependence of the radiation emitted from each of the two sources suspended in vacuum, while properly accounting for the Ampère boundary condition.

As long as rectangular mesas were the only radiation sources under study, it has proved difficult to distinguish the results of these radiation sources, as all of the observed harmonics can be amplified by the cavity features of the mesa[21, 23]. The extreme non-linear current-voltage characteristic of each mesa allows for chaotic, nonequilibrium effects to be important, so complications such as soliton kinks [18,19] or layer-dependent kinks [9-14] could potentially play important roles in the origin of the radiation. As noted above, additional rectangular cavity modes might form across the length of the sample[22]. The only practical ways to distinguish these models in rectangular mesas is by the observations of the angular dependence of the output power, polarization, and coherence fraction. As indicated previously[23], the antisymmetric cavity model necessarily leads to a maximum in the radiation intensity at $\theta = 0°$, directly above the mesa, whereas the conducting dipole antenna model leads to zero radiation intensity at $\theta = 0°$. The situation near $\theta = 90°$ is much less clear. The conducting dipole antenna model leads to a substantial radiation intensity in that direction in the absence of a superconducting substrate. However, depending upon the index of refraction of the mesa, emission from the cavity model can lead either to a vanishing or a non-vanishing output at $\theta = 90°$ for a non-superconducting substrate. Thus,

m	χ_{m1}	χ_{m2}	χ_{m3}	χ_{m4}	χ_{m5}	χ_{m6}
0	3.8317	7.0156	10.1735	13.3237	16.4706	19.6159
1	1.8412	5.3314	8.5363	11.7060	14.8636	18.0155
2	3.0542	6.7061	9.9695	13.1704	16.3475	19.5129
3	4.2012	8.0152	11.3459	14.5858	17.7887	20.9725
4	5.3176	9.2824	12.6819	15.9641	19.1960	22.4010
5	6.4156	10.5199	13.9872	17.3128	20.5755	23.8036
6	7.5013	11.7349	15.2682	18.6374	21.9317	25.1839
7	8.5778	12.9324	16.5294	19.9419	23.2681	26.5450
8	9.6474	14.1155	17.7740	21.2291	24.5872	27.8893
9	10.7114	15.2867	19.0046	22.5014	25.8913	29.2186
10	11.7709	16.4479	20.2230	23.7607	27.1820	30.5345

TABLE I: Table of the first six wave vector parameters $\chi_{mp} = k'_{mp}a$ for $m = 0, \ldots, 10$, where p defines the rank ordering of the non-vanishing values of $J'_m(\chi_{mp}) = 0$, for a thin cylindrical cavity of radius a.

it is important to study a different experimental configuration, in which more substantial differences between the output predictions of these two models would be clearly evident. It is also crucial to consider the effects of the superconducting substrate.

C. Cylindrical mesas

Here the application of these two models to mesas with cylindrical geometry, which recently have been studied experimentally [26], is described. Hu and Lin numerically studied the radiation from cylindrical mesas suspended in vacuum [13, 14, 27]. In place of Eq. (2), the mode frequencies for a thin cylindrical cavity of radius a and height $h \ll a$ with the correct Love boundary condition $H_\phi(\rho' = a) = 0$, are given by

$$k'_{mp} = \chi_{mp}/a, \tag{5}$$

$$\nu_{mp} = \frac{ck'_{mp}}{2\pi n_r} = \frac{c\chi_{mp}}{2\pi a n_r}, \tag{6}$$

where the anharmonic $\chi_{mp} = k'_{mp}a$ values are listed in Table I. From fits to three cylindrical mesas[26], the choice $n_r \approx \sqrt{18}$ fit the assumption that the fundamental *ac* Josephson frequency locked onto the cavity (11) mode reasonably well, as it did in fitting the rectangular cavity (10) mode on many samples[1, 2, 21]. Hence, in numerical calculations, the value $n_r = \sqrt{18}$ for the frequencies of interest shall be used.

Although a layered superconductor consists of a stack of Josephson junctions that in some circumstances may behave rather independently[28], here it is assumed that under the application of a *dc* voltage V_0 across the N layers, all of the layers behave identically. This assumption was also made by Tachiki *et al.*[18], and is consistent with the conclusions of Bulaevskii and Koshelev [6–8], but is distinctly different from that made by Hu and Lin[9–14]. For the electric dipole antenna model, the frequencies of the emitted radiation are the same as those present in the *ac* Josephson current, $\nu_n = n\nu_J$, since the integer harmonics are generated by the nonlinear *ac* Josephson effect. For a cylindrical cavity obeying the linear electrodynamics of Maxwell's equations, however, the frequencies ν_{mp} of the amplified radiation are the non-vanishing values generated by the pth zeroes of the first derivatives of the mth regular Bessel functions $J_m(z)$, which are far from integer multiples of one another, as illustrated in Table I. If a particular cavity mode were to come in resonance with the fundamental *ac* Josephson frequency ν_J, then higher harmonics of the Josephson current would not be resonant with any other cylindrical cavity mode, and could not be amplified by the linear electromagnetic cavity obeying Maxwell's equations. Hypothetically, if some cavity modes did not require resonance with the Josephson current to radiate, the frequency spectrum of the emitted radiation would be distinctly nonharmonic, as pictured by Hu and Lin[14]. Hence, if resonance of the fundamental *ac* Josephson current frequency with a non-uniform cylindrical cavity mode were the only way that the radiation could occur, one would not expect to observe any higher harmonics in the output power. Observation of higher harmonics would therefore be *prima facie* evidence that a substantial amount of the radiation does not directly arise from the excitation and amplification of cylindrical cavity modes.

Here the angle and frequency dependencies of the output power for both the cavity and electric dipole models for cylindrical and rectangular mesas are calculated. It is shown that the experiments on cylindrical mesas presented by Tsujimoto *et al.* provided strong evidence that the radiation at the fundamental *ac* Josephson frequency, consistent with

the (11) cylindrical cavity mode, is a mixture obtained from both the electric and magnetic current sources[26]. To fit the data quantitatively, one must also take account of the dramatic effects of the superconducting substrate. In particular, the higher frequencies observed in the measured output power are *harmonics* (*i. e.*, integral multiples) of the fundamental, and cannot arise from the excitations of higher cavity modes. Studies of the angular dependence of the power, polarization, and coherence of the emission at the fundamental frequency may help to separate the two radiation sources, as well. For rectangular mesas, the corners make the correct boundary condition $B_{||} = 0$ at the mesa edge difficult to impose. However, with the Love equivalence principles, one can find a closed form expression for the far-field radiation, the results of which are also presented.

The paper is organized as follows. In Secs. II-VI, the radiation emitted from cylindrical cavities is studied theoretically, since the results for this geometry are the simplest. In Sec. II, the primary radiation source, the *ac* Josephson current, is studied. In Sec. III, the radiation intensity from an excited cavity mode alone is calculated. In Sec. IV, the output power of the combined primary and excited cavity mode secondary radiation is calculated. In Sec. V, the electric polarization and coherence of this combined radiation is calculated and discussed. In Sect. VI, the effects of superconducting substrates are treated and discussed. In Sec. VII, analogous results for rectangular mesas are presented. The overall results are discussed and summarized in Sec. VIII.

II. PRIMARY CYLINDRICAL MESA RADIATION SOURCE

The intrinsic non-linearity of the Josephson junctions causes the *ac* Josephson current to have a large number of harmonics at $\nu_n = n\nu_J$, where $\nu_J = \omega_J/(2\pi)$, and ω_J is given by Eq. (1). This occurs regardless of the spatial dependence of the Josephson current within each junction. From Love's magnetic equivalence principle, $\boldsymbol{H}(\boldsymbol{x}', t)$ in the cavity generated by the *ac* Josephson current along $\hat{\boldsymbol{z}}'$ according to Ampère's law generates radiation that is treated by replacing it with a surface electric current source $\boldsymbol{J}_S$, and setting the resulting tangential component $H_{||}$ of $\boldsymbol{H}(\boldsymbol{x}', t)$ at the surface of the mesa equal to zero[3, 4, 25]. This *ac* Josephson current has two essential functions in the radiation. First, it radiates at all of its harmonic frequencies. Second, the radiation at one of its frequencies may lock onto that of a cylindrical cavity mode, exciting it, and causing it to radiate as well. Hence, the

ac Josephson current is the primary radiation source. For simplicity, one may assume that during emission, all or most of the N junctions have synchronized and radiate together[21], so one may neglect the layer index of the spatial variation[28], and write within the mesa

$$\boldsymbol{J}(\boldsymbol{x}',t) \;=\; \hat{\boldsymbol{z}}' \sum_{n=1}^{\infty} e^{-in\omega_J t}[J_n^J + \delta J_n(\boldsymbol{x}')], \tag{7}$$

where $\langle \delta J_n(\boldsymbol{x}') \rangle$, the spatial average of $\delta J_n(\boldsymbol{x}')$ within the mesa, vanishes. It is assumed that any time dependence to $\delta J_n(\boldsymbol{x}')$ is slow with respect to the measurement times, and can be neglected.

One may assume that no radiation emanates from the top and bottom surfaces of the cylindrical mesa. This leads to the surface electric current density, which may be written just inside the cylindrical mesa edge as

$$\boldsymbol{J}_S(\boldsymbol{x}',t) \;=\; \frac{a}{2}\eta(z')\delta(\rho'-a)\boldsymbol{J}(\boldsymbol{x}',t), \tag{8}$$

where $\boldsymbol{J}(\boldsymbol{x}',t)$ is given by Eq. (7) and $\eta(z') = \Theta(z')\Theta(h-z')$. For $h/a \ll 1$, it suffices to take $\eta(z') \to h\delta(z')$ when the mesa is suspended in vacuum. A sketch of the uniform part of the surface electric current density $\boldsymbol{J}_S$ at the edge of a cylindrical mesa is given in Fig. 1.

For the full set of harmonic *ac* Josephson frequencies, the magnetic vector potential $\boldsymbol{A}(\boldsymbol{x},t)$ is given by

$$\boldsymbol{A}(\boldsymbol{x},t) \;=\; \frac{a\mu_0}{8\pi} \sum_{n=1}^{\infty} \int d^3\boldsymbol{x}' \hat{\boldsymbol{z}}' \eta(z')\delta(\rho'-a) \frac{e^{in(k_J R - \omega_J t)}}{R}[J_n^J + \delta J_n(\boldsymbol{x}')], \tag{9}$$

where $R = |\boldsymbol{x} - \boldsymbol{x}'|$. Although ω_J must be the same inside and outside the mesa, $k_J = \omega_J/c$ outside the mesa must match the wave vector of light in vacuum, whereas inside the mesa, $k_J' = n_r\omega_J/c$. Since $\boldsymbol{A}||\hat{\boldsymbol{z}}$ is parallel to the mesa edge, this wave vector change at the boundary automatically satisfies the Maxwell boundary condition that the tangential components of $\boldsymbol{E}$ are preserved across the boundary. One may then write

$$\boldsymbol{A}(\boldsymbol{x},t) \;=\; \boldsymbol{A}_J(\boldsymbol{x},t) + \boldsymbol{A}_{\delta J}(\boldsymbol{x},t), \tag{10}$$

separating it into its contributions from the spatially uniform J_n^J and inhomogeneous $\delta J_n(\boldsymbol{x}')$ source amplitudes. In the Appendix, a theory for $\delta J_n(\boldsymbol{x}')$ is presented.

In the far field, or radiation zone, $r/a \gg 1$, one may use the standard approximation

$$\frac{e^{ikR}}{R} \;\to\; \frac{e^{ikr}}{r} e^{-i\boldsymbol{k}\cdot\boldsymbol{x}'}, \tag{11}$$

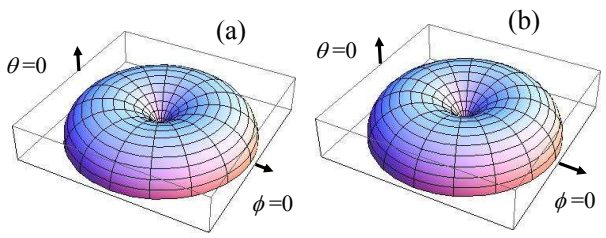

FIG. 2: (Color online) Plots of the radiation intensity in arbitrary units emitted from the uniform J_n^J part of the *ac* Josephson current when a cylindrical mesa is suspended in vacuum. (a) The radiation at the fundamental $n = 1$ mode. (b) The radiation at the $n = 2$ second harmonic mode.

where $|\boldsymbol{x}| = r$ and $\hat{\boldsymbol{z}}' \rightarrow -\hat{\boldsymbol{\theta}} \sin\theta$ in spherical coordinates, and inside the mesa, $\boldsymbol{k} \cdot \boldsymbol{x}' = k\rho' \sin\theta \cos(\phi - \phi')$ in cylindrical coordinates [3–5]. The integral in Eq. (9) is readily evaluated, leading to $\boldsymbol{E_A} = -\frac{\partial \boldsymbol{A}}{\partial t}$ and $\boldsymbol{H_A} = \frac{1}{\mu_0} \boldsymbol{\nabla} \times \boldsymbol{A}$. In the radiation zone, the uniform contribution $\boldsymbol{E}_{\boldsymbol{A}_J}$ from $\boldsymbol{A}_J$ to $\boldsymbol{E_A}$ is given by

$$\boldsymbol{E}_{\boldsymbol{A}_J}(\boldsymbol{x}, t) \underset{r/a \gg 1}{\rightarrow} -\frac{i\hat{\boldsymbol{\theta}} \sin\theta v \mu_0}{4\pi r} \sum_{n=1}^{\infty} e^{in(k_J r - \omega_J t)} n J_n^J \omega_J J_0(nk_\theta) S_n^J(\theta), \tag{12}$$

where $v = \pi a^2 h$ is the volume of the mesa, $k_\theta = k_J a \sin\theta$, $J_0(z)$ is a regular Bessel function, and $S_n^J(\theta) = 1$ for a sample suspended in vacuum. The radiation from the surface electric current source is linearly polarized with $\boldsymbol{E}_{\boldsymbol{A}_J} || \hat{\boldsymbol{\theta}}$. So far, however, $k_J = \omega_J / c$ is only determined by the applied V_0/N, and is unspecified with respect to the mesa dimensions. When the fundamental *ac* Josephson mode frequency ν_J locks onto the (mp) cavity mode frequency, the resulting k'_J and k_J values are given by $k'_J = \omega_J n_r / c = \chi_{mp}/a$ inside the BSCCO mesa, and $k_J = \omega_J / c = \chi_{mp}/(a n_r)$ in vacuum outside the mesa.

The radiation-zone intensity $\mathcal{I}(\theta, \phi)$ for the conducting dipole model is given by the differential power per unit solid angle $dP/d\Omega = \frac{1}{2}\mathrm{Re}[r^2 \hat{\boldsymbol{r}} \cdot \overline{\boldsymbol{E} \times \boldsymbol{H}^*}]$[5], where $\overline{\cdots}$ is a time average. The contribution to $dP/d\Omega$ from the uniform J_n^J source in the radiation zone is

$$\frac{dP_J}{d\Omega} \underset{r/a \gg 1}{\rightarrow} \sin^2\theta \sum_n |B_n(\theta) J_0(nk_\theta)|^2, \tag{13}$$

where $B_n(\theta) = J_n^J v S_n^J(\theta) n k_J \sqrt{Z_0}/(4\sqrt{2}\pi)$, and $Z_0 = \sqrt{\mu_0/\epsilon_0}$ is the vacuum impedance. The radiation patterns expected with $k_J a = \chi_{11}/n_r \approx 1.8412/n_r$ from the uniform part of the conducting dipole model alone at the fundamental ($n = 1$) and second harmonic ($n = 2$) when the mesa is suspended in vacuum are pictured in Figs. 2(a) and 2(b), respectively. These $\mathcal{I}(\theta, \phi)$ patterns are nearly indistinguishable, except for their emission frequencies, due

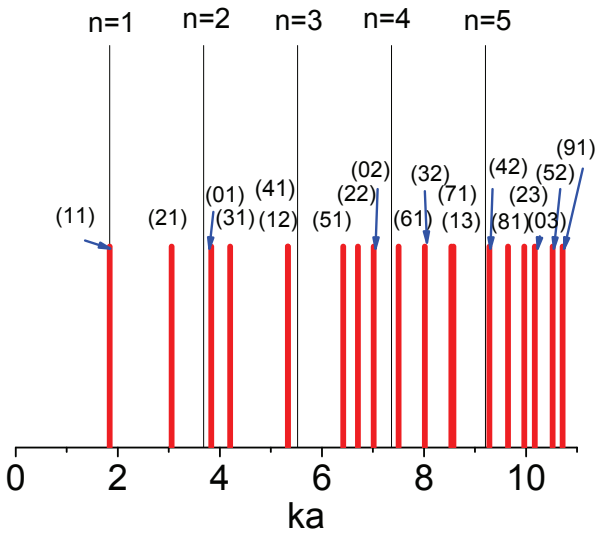

FIG. 3: (Color online) Sketch of the lowest five wave vectors of the *ac* Josephson current harmonics (long thin black) and the lowest 19 cylindrical cavity modes (short thick red), assuming the fundamental ($n = 1$) *ac* Josephson frequency locks onto the lowest energy (11) cavity mode frequency. The (mp) indices of the cavity modes are indicated.

to their long wavelengths in vacuum relative to the mesa size. The $\mathcal{I}(\theta, \phi)$ vanish at $\theta = 0°$, due to the geometric factor $\sin\theta$ in the radiation-zone spherical coordinate representation of $\hat{\boldsymbol{z}}'$, are independent of ϕ, and exhibit a maximum at $\theta = 90°$, as for ordinary electric dipole radiation from a quasi-one-dimensional wire or thin rod-shaped source.

III. RADIATION FROM A CYLINDRICAL CAVITY MODE

From Table I and the calculations in the Appendix, we assume the lowest energy (11) cylindrical cavity mode frequency locks onto the fundamental *ac* Josephson frequency. The other cylindrical cavity mode frequencies are then far from the harmonic frequencies in the *ac* Josephson current, as sketched in Fig. 3. Let us now study the angular dependence of the radiation, assuming that a particular cavity mode $(mp) = (m_0 p_0)$ is excited and radiates. After equilibrium has been achieved, the electric field in the cavity is obtained from the displacement current, the most important part of which arises from the resonant part of the particular solution $A_z^{(p)}(\boldsymbol{x}', t)$ to the inhomogeneous wave equation for $A_z(\boldsymbol{x}', t)$ studied in

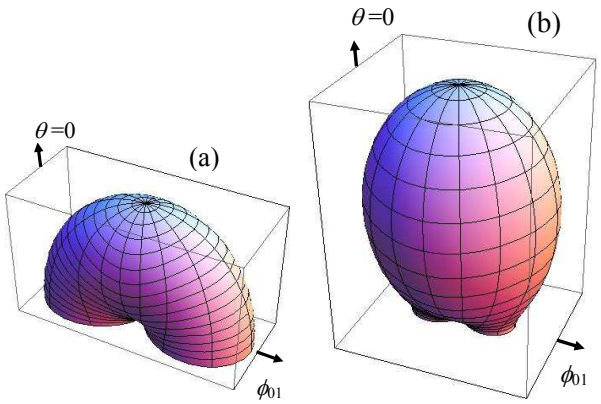

FIG. 4: (color online) Plots of the radiation intensity in arbitrary units emitted from cavity modes when the mesa is suspended in vacuum. (a) The cavity (11) mode with $k_{11}a = 1.8412/n_r$. (b) The cavity (12) mode with $k_{12}a = 5.3314/n_r$.

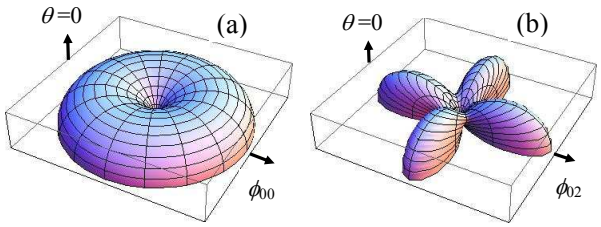

FIG. 5: (Color online) Plots of the radiation intensity in arbitrary units emitted from cavity modes when the mesa is suspended in vacuum. (a) The cavity (01) mode with $k_{01}a = 3.8317/n_r$. (b) The cavity (21) mode with $k_{21}a = 3.0542/n_r$.

the Appendix. Then, $\boldsymbol{M}_S(\boldsymbol{x}', t) = -\hat{\boldsymbol{n}} \times \boldsymbol{E}^{(p)}(\boldsymbol{x}', t)|_S$, [3, 4, 25] where $\hat{\boldsymbol{n}} = \hat{\boldsymbol{\rho}}'$, is

$$\boldsymbol{M}_S(\boldsymbol{x}', t) \;=\; -\hat{\boldsymbol{\phi}}' \frac{a}{2} \eta(z') \delta(\rho' - a) \frac{\partial A_z^{(p)}(\boldsymbol{x}', t)}{\partial t}, \tag{14}$$

where $\eta(z')$ is given following Eq. (8) for a sample suspended in vacuum.

For a single frequency ω and wave vector k, the electric vector potential $\boldsymbol{F}(\boldsymbol{x}, t)$ outside the sample is

$$\boldsymbol{F}(\boldsymbol{x}, t) \;=\; \frac{\epsilon_0}{4\pi} \int d^3\boldsymbol{x}' \boldsymbol{M}_S(\boldsymbol{x}', t) e^{ikR}/R, \tag{15}$$

where $\boldsymbol{M}_S(\boldsymbol{x}', t)$ is evaluated at $\omega = ck$[3–5].

The generalized $\boldsymbol{F}(\boldsymbol{x}, t)$ is then obtained from Eq. (15) by replacing ω with $\omega_{m_0 p_0} = n\omega_J$, as described in the Appendix. Using the Schelkunoff expression for the electric field, $\boldsymbol{E}_{\boldsymbol{F}} =$

$-\frac{1}{\epsilon_0}\boldsymbol{\nabla}\times\boldsymbol{F}$, the resonant contribution $\boldsymbol{E}_{\boldsymbol{F}_{\rm r}}$ to $\boldsymbol{E}_{\boldsymbol{F}}$ in the radiation zone is

$$\boldsymbol{E}_{\boldsymbol{F}_{\rm r}}(\boldsymbol{x},t) \underset{r/a\gg 1}{\rightarrow} -(-i)^m G^{(n)}_{mp}\frac{e^{i(k_{mp}r-\omega_{mp}t)}}{4\pi r}\delta_{n\omega_J,\omega_{mp}}\{\hat{\boldsymbol{\phi}}\cos\theta\sin[m(\phi-\phi_{0n})]J^+_m(k^\theta_{mp}) + \hat{\boldsymbol{\theta}}\cos[m(\phi-\phi_{0n})]J^-_m(k^\theta_{mp})\}\Big|_{\substack{p=p_0\\m=m_0}}, \tag{16}$$

$$G^{(n)}_{mp} = \frac{v}{2\epsilon}k_{mp}t_{\rm eff}C^{(n)}_{mp}J_m(k'_{mp}a)S^M_{mp}(\theta), \tag{17}$$

where $J^\pm_m(z)=[J_{m+1}(z)\pm J_{m-1}(z)]/2$, $k^\theta_{mp}=k_{mp}a\sin\theta$, and the ϕ_{0n} are constants describing $\delta J_n(\boldsymbol{x}')$, $S^M_{mp}(\theta)=1$ for a sample suspended in vacuum, as detailed in the Appendix. The magnetic field $\boldsymbol{H}_{\boldsymbol{F}_{\rm r}}$ at the resonant frequency may be obtained from $-\frac{\partial \boldsymbol{H}_{\boldsymbol{F}_{\rm r}}}{\partial t}=\boldsymbol{\nabla}\times\boldsymbol{E}_{\boldsymbol{F}_{\rm r}}$. The overall factor $-(-i)^m$ in $\boldsymbol{E}_{\boldsymbol{F}_{\rm r}}$ plays a very important role when $\boldsymbol{E}_{\boldsymbol{A}_J}$ is added to $\boldsymbol{E}_{\boldsymbol{F}_{\rm r}}$, as discussed in Sec. IV.

One may then calculate the output power of the (m_0p_0) cavity mode in the radiation zone, which is averaged over t after the resonance has saturated. Some or all of the ϕ_{0n} might vary with experimental run, in which case an average of the output power over all possible ϕ_{0n} values might be warranted. One then obtains

$$\frac{dP_{m_0p_0}}{d\Omega} \underset{r/a\gg 1}{\rightarrow} \frac{\sqrt{\epsilon}|G^{(n)}_{mp}|^2}{32\pi^2}\Big[\Big(\cos[m(\phi-\phi_{0n})]J^-_m(k^\theta_{mp})\Big)^2 + \Big(\cos\theta\sin[m(\phi-\phi_{0n})]J^+_m(k^\theta_{mp})\Big)^2\Big]\Big|_{\substack{p=p_0\\m=m_0}}. \tag{18}$$

In the radiation zone, spherical plots of the radiation intensity $\mathcal{I}(\theta,\phi)$ patterns for the four TM^z_{mp} cavity modes with the lowest energies and with ϕ_{0n} fixed are shown for a cylindrical mesa suspended in vacuum in Figs. 4-5. For fixed ϕ_{0n}, the radiation patterns all possess C_{2mv} point group symmetry, exhibiting invariance under rotations of π/m about the $\theta=0^\circ$ axis and $2m$ mirror planes containing that axis. For $m=0$, the point group symmetry is denoted as $C_{\infty v}$, as it is rotationally invariant about $\theta=0^\circ$. The far-field radiation from the $m=1$ cavity modes, two $\mathcal{I}(\theta,\phi)$ of which are pictured in Fig. 4, exhibit absolute maxima at $\theta=0^\circ$ and a substantial azimuthal (ϕ) anisotropy with a substantial azimuthal average for the (11) mode pictured in Fig. 4(a) near $\theta\approx 90^\circ$, where the output from the experiments appears to vanish[26]. When the mesa is suspended in vacuum, the contributions to $\mathcal{I}(\theta,\phi)$ from all other cavity modes, such as the (01) and (21) modes pictured in Fig. 5, vanish at $\theta=0^\circ$, unlike the experimental observations[26]. All cavity modes emitted from mesas suspended in vacuum have large outputs for $\theta=90^\circ$. $\mathcal{I}(\theta,\phi)$ of the cavity (01) mode pictured in Fig. 5(a) is independent of ϕ, and is very similar to that of the *ac* Josephson $n=2$ mode

pictured in Fig. 2(b). Hu and Lin presented very similar results for the output from the cavity modes pictured in Figs. 4-5 [14, 27].

IV. COMBINED PRIMARY AND SECONDARY RADIATION

When both electric and magnetic surface current sources make significant contributions to the radiation, one may use the Schelkunoff procedure of adding the electric and magnetic fields from the two sources, $\boldsymbol{E} = \boldsymbol{E_A} + \boldsymbol{E_F}$ and $\boldsymbol{H} = \boldsymbol{H_A} + \boldsymbol{H_F}$[3, 4]. The main contributions to $\boldsymbol{E_A}$ and $\boldsymbol{H_A}$ are $\boldsymbol{E_{A_J}}$ and $\boldsymbol{H_{A_J}}$, arising from the uniform part of the *ac* Josephson current. The main contributions to $\boldsymbol{E_F}$ and $\boldsymbol{H_F}$ are $\boldsymbol{E_{F_r}}$ and $\boldsymbol{H_{F_r}}$, arising from the excitation of a cavity mode (or modes, for rectangular mesas). The combined $dP/d\Omega$ is then computed using $\boldsymbol{E}$ and $\boldsymbol{H}$ as described just prior to Eq. (13).

After equilibrium has been achieved, one may assume that the fundamental $n = 1$ *ac* Josephson frequency has locked onto that of the cavity $(m_0 p_0) = (11)$ mode, with the wave vector amplitude $k_{11}a = 1.8412/n_r$, as observed for three cylindrical mesas[26]. The combined far-field electric field from its main contributions $\boldsymbol{E} = \boldsymbol{E_{A_J}} + \boldsymbol{E_{F_r}}$ then has the components

$$E_\theta = i[G_{11}^{(1)} \cos(\phi - \phi_{01}) J_1^-(k_\theta) - \overline{B}_1 \sin\theta J_0(k_\theta)] \frac{e^{i(k_J r - \omega_J t)}}{4\pi r}, \tag{19}$$

$$E_\phi = i G_{11}^{(1)} \cos\theta \sin(\phi - \phi_{01}) J_1^+(k_\theta) \frac{e^{i(k_J r - \omega_J t)}}{4\pi r}, \tag{20}$$

$$\overline{B}_n = n v \mu_0 \omega_J J_n^J S_n^J(\theta), \tag{21}$$

and $G_{11}^{(1)}$ is given by Eq. (17). The components to E_θ from $\boldsymbol{E_{A_J}}$ and $\boldsymbol{E_{F_r}}$ are either in phase or out of phase by π, depending upon ϕ_{01}.

The combined $dP_{11}/d\Omega$ of the fundamental $n = 1$, spatially homogeneous *ac* Josephson surface current density frequency locked onto that of the cavity (11) mode at $\omega_J = \omega_{11}$ is given in the radiation zone by

$$\frac{dP_{11}}{d\Omega} \underset{r/a \gg 1}{\rightarrow} \frac{\sqrt{\epsilon}}{32\pi^2} \Big[\Big| G_{11}^{(1)} \cos\theta \sin(\phi - \phi_{01}) J_1^+(k_\theta) \Big|^2 + \Big| G_{11}^{(1)} \cos(\phi - \phi_{01}) J_1^-(k_\theta) - \overline{B}_1 \sin\theta J_0(k_\theta) \Big|^2 \Big], \tag{22}$$

where $k_\theta = k_J a \sin\theta$. Note that the fully coherent output power is asymmetric in ϕ, lowering the C_{2v} point group symmetry to C_1, with a single mirror plane normal to the substrate

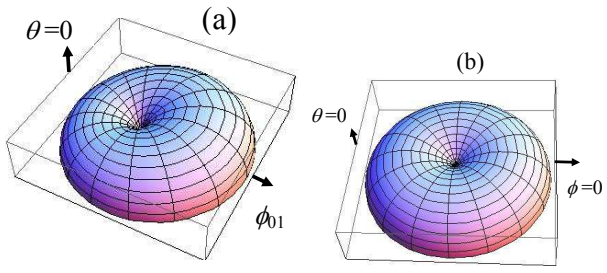

FIG. 6: (Color online) Plots of the radiation power emitted from the mixed $n = 1$ *ac* Josephson and (11) cavity (11) mode with ϕ_{01} fixed and $k_{11}a = 1.8412/n_r$ for the mesa suspended in vacuum. (a) $|\overline{B}_1/G_{11}^{(1)}| = 5$ and is ϕ_{01} fixed as indicated. (b) $|\overline{B}_1/G_{11}^{(1)}| = 7$ and ϕ_{01} is random.

that contains ϕ_{01}. A plot of the combined output $\mathcal{I}(\theta, \phi)$ from Eq.(22) for $|\overline{B}_1/G_{11}^{(1)}| = 5$ when ϕ_{01} is fixed and the mesa is suspended in vacuum is shown in Fig. 6(a). The output power in Fig. 6(a) is finite at both $\theta = 0°$ and $\theta = 90°$.

A plot of $\mathcal{I}(\theta, \phi)$ for the incoherently combined $n = 1$ dipole and (11) cavity modes with ϕ_{01} random and $|\overline{B}_1/G_{11}^{(1)}| = 7$ is shown in Fig. 6(b). Averaging over ϕ_{01} has a drastic effect on the output point group symmetry, which is now $C_{\infty v}$, exhibiting rotational invariance about $\theta = 0°$. Such an incoherent combination was successfully used in fits to experimental data on cylindrical mesas [25]. As seen in Sec. V, it also has an effect on the polarization.

In fits to the data, the total integrated power is $P_{11} = 2\pi \int_0^{\pi/2} \sin\theta d\theta dP_{11}(\theta)/d\Omega$, where $dP_{11}/d\Omega$ was averaged over ϕ_{01}[26], and the coefficients $B_1(\theta)$ and $G_{11}^{(1)}(\theta)$ were both taken to be proportional to $\cos\theta$ for a sample on a superconducting substrate, as discussed in Sec. VI. P_{11} then has the form $A + B\alpha(0)$, where $\alpha(0) = |B_1(0)/G_{11}^{(1)}(0)|$, and the fraction of the radiation arising from the uniform *ac* Josephson current source is $[1 + (B/A)\alpha(0)]^{-1}$[26].

V. ELECTRIC POLARIZATION OF THE COMBINED RADIATION

The electric polarization of the combined output at the fundamental frequency $\omega_J = \omega_{11}$ and $k_J = k_{11}/n_r$ is more interesting. The radiation of the combined Josephson $n = 1$ fundamental frequency locked onto that of the cavity (11) mode generally has linear polarization, the direction of which generally depends upon (θ, ϕ). Some special cases are: (I) If ϕ_{01} is random during the measurement, the radiation is linearly polarized along $\hat{\boldsymbol{\theta}}$, arising from the dipole radiation only. This vanishes at $\theta = 0°$, where the radiation is unpolarized.

(II) If $\phi - \phi_{01} = 0, \pi$, the polarization is along $\hat{\boldsymbol{\theta}}$. (III) If $\theta = 0°$, the polarization direction depends strongly upon $\phi - \phi_{01}$. But in a measurement at $\theta = 0°$, one would integrate over all ϕ values, measuring an unpolarized radiation, in agreement with experiment[26]. (IV) If $\theta = 90°$, the radiation is linearly polarized along $\hat{\boldsymbol{\theta}}$. (V) There is in addition one line given by

$$\phi - \phi_{01} \;=\; \cos^{-1}\Big(\frac{|\overline{B}_1|\sin\theta J_0(k_\theta)}{|G_{11}^{(1)}|J_1^-(k_\theta)}\Big), \tag{23}$$

where $E_\theta = 0$ and the polarization is along $\hat{\boldsymbol{\phi}}$. For the general case, the polarization is tilted away from the $\hat{\boldsymbol{\theta}}$ direction by the angle τ given by[3, 4]

$$\tau \;=\; \tan^{-1}\Big(\frac{E_\phi}{E_\theta}\Big). \tag{24}$$

In Fig. 7, three-dimensional plots of $2\tau/\pi$ in radians versus θ in degrees and $r = |\overline{B}_1/G_{11}^{(1)}|$ for $\phi - \phi_{01} = \pi/2$ and $\phi - \phi_{01} = \pi/4$ in the left and right panels are respectively presented. In Fig. 7(a), when $\phi - \phi_{01} = \pi/2$, E_θ is only given by the *ac* Josephson (or dipole) radiation, which vanishes in the limits $\theta = 0°$ and $r = 0$. When $\theta = 90°$, as long as $r > 0$, the polarization is along $\hat{\theta}$. From this figure, it is evident that when $r \approx 1$ or greater and $\theta \approx 10°$ or greater, $\tau \approx 0$, and the polarization lies along $\hat{\boldsymbol{\theta}}$. In Fig. 7(b), when $\theta = 0°$ or $r = 0$, the polarization is -45° between $\hat{\boldsymbol{\phi}}$ and $\hat{\boldsymbol{\theta}}$. Then, as either $r \approx 1$ and $\theta \approx 10°$, the polarization switches to the $\hat{\boldsymbol{\theta}}$ direction, assuming the coherent combination with ϕ_{01} fixed during the measurement. If ϕ_{01} is random, the polarization is always along $\hat{\boldsymbol{\theta}}$, except at $\theta = 0°$, where it is unpolarized. Preliminary measurements confirmed the unpolarized radiation at $\theta = 0°$[26]. However, that single experiment cannot distinguish whether ϕ_{01} is fixed or random, because at $\theta = 0°$, the polarization averages to zero, both for fixed and random ϕ_{01}. Measurements of the polarization and the degree of coherence for $\theta \neq 0°$ could distinguish these possibilities.

VI. SUPERCONDUCTING SUBSTRATES

Here it is argued that the *ac* Meissner effect in the superconducting substrate sketched in Fig. 8(a) causes it to behave as a perfect magnetic conductor (PMC)[3, 4, 23], which can be treated by the image source technique as sketched in Fig. 9. The Love magnetic conductor

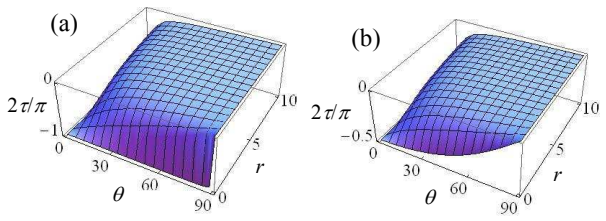

FIG. 7: (Color online) Plots of the normalized tilt angle $2\tau/\pi$ in radians of the polarization from $\hat{\boldsymbol{\theta}}$, versus θ in degrees and $r = \overline{B}_1/G_{11}^{(1)}$ of the mixed source radiation for fixed ϕ_{01} at the fundamental $n = 1$ frequency with $k_{11}a = 1.8412/n_r$ when the mesa is either suspended in vacuum or on a superconducting substrate. (a) $\phi - \phi_{01} = \pi/2$. (b) $\phi - \phi_{01} = \pi/4$. .

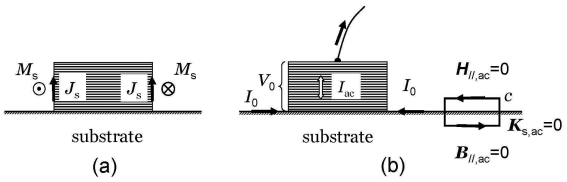

FIG. 8: (a) Sketch of a mesa with $\boldsymbol{J}_S$ and $\boldsymbol{M}_S$ surface current sources. (b) Mesa during coherent emission with applied *dc* I_0, V_0, and I_{ac} confined to it. Curve c is the integration path for the Ampère boundary condition. See text.

equivalence principle allows one to replace the magnetic field internal to the mesa by a surface electric current, and to set $H_{||} = 0$ on the surface of the mesa. Present mesa antennas atop a PMC substrate emit dramatically lower output power than those atop a substrate that is an insulator or perfect electric conductor (PEC)[3, 4]. Note that a superconducting Nb substrate was previously used as a ground plane for a square lattice of Nb/Al_2O_3 Josephson junctions, the output of which was amplified by a cavity at the edge of the array[33–35]. Without the ground plane, the radiation was not detectable. In that case, the *ac* Josephson

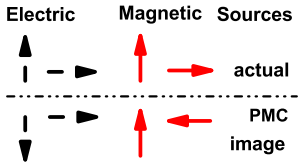

FIG. 9: (Color online) Sketches of the electric (dashed, black) and magnetic (solid, red) actual and image sources and on a perfect magnetic conductor substrate. From Ref. (3).

current source was parallel to the substrate [33–35], so that the image of the supercurrent in the PMC substrate was parallel to the source current, as sketched by the two (black, dashed) arrows second from the left in Fig. 9. In the case of BSCCO mesas atop a BSSCO substrate, both the electric and magnetic image currents are opposite to the respective source currents, as in the far left and far right arrow pairs in Fig. 9, causing a cancelation of the output power at $\theta = 90°$. This model thus can explain why $\mathcal{I}(90°, \phi)/\mathcal{I}(0°, \phi)$ is unexpectedly so small.

Here the effects of superconducting substrates are studied quantitatively[1, 2]. As sketched in Fig. 8(b), during coherent Josephson radiation, the *ac* Josephson current is essentially confined to the mesa by the applied *dc* current I_0 and voltage V_0. With only a *dc* surface current density $\propto I_0$ and $B_{||,ac}(t) = 0$ beyond the skin depth (≈ 0.15 μm) inside the BSCCO substrate due to the *ac* Meissner effect, the Ampère boundary condition forces $H_{||,ac}(t) = 0$ just above the BSCCO substrate[5]. This corresponds to a PMC substrate, with the effective image sources sketched in Fig. 9[3, 4]. Thus, for a BSCCO substrate, we restrict θ to $0° \leq \theta \leq 90°$ and replace $\eta(z')$ in Eqs. (14) and (8) by

$$\eta_-(z') \; = \; \mathrm{sgn}(z')\Theta[h^2 - (z')^2]. \tag{25}$$

For cylindrical mesas in the radiation zone, $h << a, r$, it is safe to assume $h \ll 1/k_n$ for the relevant n. One may expand e^{ik_nR}/R in Eqs. (9) and (15) for small z'. From Eq. (25), the electric and magnetic current substrate factors are simply obtained from terms linear in z'. In the radiation zone,

$$S_n^J(\theta) \underset{r\to\infty}{\to} -ik_n h\cos\theta \;\; \Theta(90° - \theta), \tag{26}$$

and $S_{mp}^M(\theta)$ is obtained from $S_n^J(\theta)$ by $k_n \to k_{mp}$, where (mp) applies to either cylindrical or rectangular cavity modes, the latter as discussed in Sec. VII.

In Figs. 10(a) and 10(b), the predictions are shown for the radiation power emitted from the mixed fundamental $n = 1$ *ac* Josephson and (11) cavity modes of a cylindrical mesa atop a superconducting substrate. In each case, the radiation vanishes at $\theta = 90°$, unlike the radiation from the same modes shown in the left panels of Figs. 2 and 4 when the mesa is suspended in vacuum. In Fig. 10(a), it was assumed that ϕ_{01} was fixed, and $|\overline{B}_1/G_{11}^{(1)}| = 7$, which maintains the point kink found for the combined output pictured in Fig. 6(a) for the mesa suspended in vacuum. In Fig. 10(a), the predicted radiation vanishes at $\theta = 90°$, but

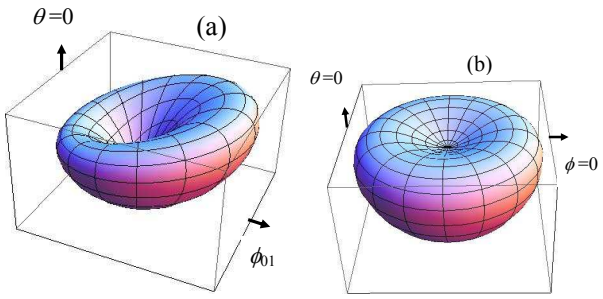

FIG. 10: (Color online) Plots of the radiation power emitted from the mixed $n = 1$ *ac* Josephson and the (11) cylindrical cavity modes with $k_{11}a = 1.8412/n_r$ fixed and the mesas sit atop a superconducting substrate. (a) ϕ_{01} is fixed as indicated, and $|\overline{B}_1/G_{11}^{(1)}| = 7$. (b) ϕ_{01} is random and $|\overline{B}_1/G_{11}^{(1)}| = 1$.

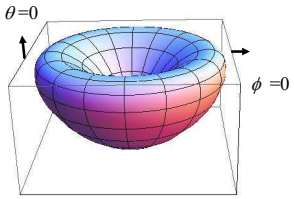

FIG. 11: (Color online) Plot of the radiation power at the $n = 2$ second harmonic of the *ac* Josephson current for a cylindrical mesa with $2k_J a = 3.6824/n_r$ on a superconducting substrate.

it is still highly anisotropic for $\theta < 90°$, with a point kink that is off center (not at $\theta = 0°$). Experiments to date cannot eliminate this possibility, because scans across the diameter of the cylinder have only been made on two perpendicular planes, and it is possible that such a point kink would have been missed. In Fig. 10(b), $|\overline{B}_1/G_{11}^{(1)}| = 1$, ϕ_{01} is random, the point kink is removed, and the output power has a maximum at $\theta \approx 34.5°$. These predictions are remarkably similar to the experimental results[26]. In Fig. 11, the modification to Fig. 2(b) for the second *ac* Josephson harmonic at $n = 2$ due to the superconducting substrate is shown. It has a maximum at $\theta \approx 42.2°$.

VII. RECTANGULAR MESAS

Let us finally reconsider the more complicated rectangular mesas. A sketch of the electric and magnetic surface current densities for the (10) rectangular mesa cavity mode is shown in Fig. 12. Although $\boldsymbol{J}_S(\boldsymbol{x}', t)$ is uniform along the edge of the mesa, $\boldsymbol{M}_{Sn}(\boldsymbol{x}', t)$ for the

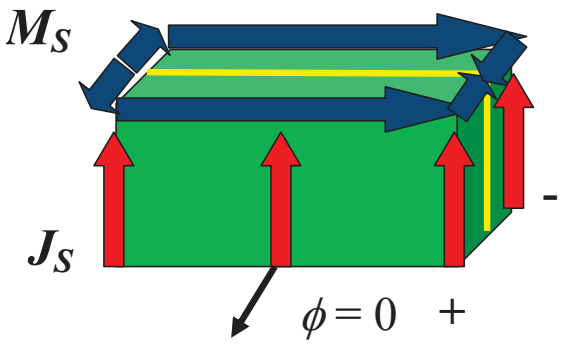

FIG. 12: (Color online) Sketch of a rectangular mesa with a surface electric current density $\boldsymbol{J}_S$ (red vertical arrows) and a magnetic current density $\boldsymbol{M}_S$ (blue horizontal azimuthal arrows). The $\pm$ signs refer to the signs of the rectangular (10) cavity mode, separated by the yellow line.

$(n0)$ mode changes its direction by 90° at each of the corners.

For a rectangular mesa of length ℓ, width w, and height h in vacuum satisfying $\ell > \lambda_c > w$, where $\lambda_c \sim 170$ μm is the c-axis penetration depth, the experimentally observed cavity modes are the TM^z_{n0} or (n0) modes, which are constant in position along the mesa height and length, and oscillate in position with integral multiples of half-wavelengths along the mesa widths[1, 2, 21]. In rectangular source coordinates (x', y', z'), the surface currents at the frequency of the $\mathrm{TM}^z_{n,0}$ mode are

$$\boldsymbol{J}_{Sn}(\boldsymbol{x}') = \hat{\boldsymbol{z}}' \frac{J^J_n}{4} \eta_J(z') \sum_{\sigma=\pm} [f_\sigma(x', y') + g_\sigma(x', y')], \tag{27}$$

$$\boldsymbol{M}_{Sn}(\boldsymbol{x}') = \frac{\tilde{E}_{0n}}{4} \eta_M(z') \sin[n(x' - x_n)\pi/w] \sum_{\sigma=\pm} \sigma[\hat{\boldsymbol{y}}' f_\sigma(x', y') - \hat{\boldsymbol{x}}' g_\sigma(x', y')], \tag{28}$$

$$f_\sigma(x', y') = w\delta(x' + \sigma w/2)\Theta[(\ell/2)^2 - (y')^2], \tag{29}$$

$$g_\sigma(x', y') = \ell\delta(y' + \sigma\ell/2)\Theta[(w/2)^2 - (x')^2], \tag{30}$$

where the TM^z_{n0} cavity mode energy is degenerate for $-w/n \leq x_n \leq w/n$.

One may treat the output power obtained from the combination of the $\boldsymbol{J}_S$ and $\boldsymbol{M}_{Sn}$ sources in three models. In the first model, one treats the combination as coherent, satisfying $H_y(x' = \pm w/2) = 0$. This leads to one of the solutions $x_n = 0, w/n$ for n odd, and one of the solutions $x_n = \pm w/2n$ for n even. These cases lead to an asymmetry and kinks in the angular distribution of the output power. In Models I and II discussed in the Appendix, the output from the two sources is incoherent.

The time-averaged $dP/d\Omega$ in the radiation zone is

$$\frac{dP}{d\Omega} \underset{r/a\to\infty}{\to} \frac{Z_0(\tilde{v}k_1)^2}{128\pi^2}\sum_{n=1}^{\infty} n^2\Big[\Big|\sin\theta J_n^J\chi_n(\theta,\phi)S_n^J(\theta)\Big|^2 + \alpha_n(\theta)\Big(C_n^i + D_n^i - \sin^2\theta[C_n^i\cos^2\phi + D_n^i\sin^2\phi - E_n^i\sin\phi\cos\phi]\Big)\Big], \quad (31)$$

where i = I, II, $\alpha_n(\theta) = |\tilde{E}_{0n}S_n^M(\theta)|^2/(2Z_0)^2$, and $\chi_n(\theta,\phi)$ and the $C_n^i(\theta,\phi)$, $D_n^i(\theta,\phi)$, and $E_n^i(\theta,\phi)$ are given in the Appendix. The results for the angular dependence of the output power from rectangular mesas are shown in Figs. 13 - 15. These figures are for rectangular mesas with the length normal to $\phi = 0$. Although the figure "boxes" appear to have the short length along $\phi = 0$, that is the direction in which the radiation is largest. Since these figures correspond to the $(n0)$ modes for $n = 1, 2$, the radiation is primarily along the length of the mesa, along or near to $\phi = 0$. In the figures that follow, it is assumed that $\ell/w = 20/3$, as in some of the mesas[1, 2]. Three-dimensional plots of $\mathcal{I}(\theta,\phi) \propto dP(\theta,\phi)/d\Omega$ in arbitrary units are then obtained. First, the data are presented for the emission from the primary source, the *ac* Josephson current in the form of the surface electric current density $\boldsymbol{J}_S$. In Fig. 13, the predicted $\mathcal{I}(\theta,\phi)$ is shown for the $n = 1$ and $n = 2$ *ac* Josephson radiation, respectively for the mesa suspended in vacuum. The corresponding predictions for the rectangular cavity (10) and (20) modes at the same frequencies as the $n = 1, 2$ *ac* Josephson radiation are shown for Model I in Fig. 14 for the cavity suspended in vacuum. Note that the output for the rectangular cavity (10) mode pictured in Fig. 14(a) is very similar to that for the cylindrical cavity (11) pictured in Fig. 4(a) when both mesas are suspended in vacuum. The angular dependence of the second harmonic emitted from rectangular cavities should be very interesting to measure, especially as it contains a mixture of the radiation predicted in Figs. 13(b) and 14(b), and is distinctly different from that from any of the cylindrical cavity modes calculated without a substrate.

In Fig. 15, the combined output from the primary *ac* Josephson current and excited cavity modes for a rectangular mesa atop a superconducting substrate are shown. In Fig. 15(a), the fundamental $n = 1$ mode is locked onto the rectangular cavity (10) mode, and the figure assumes $\alpha_1(0) = 0.2$ using Model I for the cavity. This figure is very similar to that observed experimentally[21]. In Fig. 15(b), the predicted output power is shown for the second harmonic, again using Model I with $\alpha_2(0) = 0.2$ for a mesa atop a superconducting substrate. The total output power is $P = \int_0^{2\pi} d\phi \int_0^{\pi/2} \sin\theta d\theta [dP(\theta,\phi)/d\Omega]$, leading to an expression of the form $A' + \alpha(0)B'$, where A' and B' depend upon w, ℓ, and ϵ and n. With

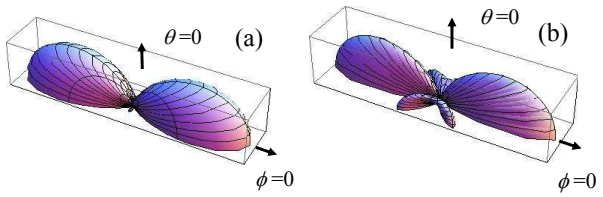

FIG. 13: (Color online) Three-dimensional plots of the radiation intensity in arbitrary units for rectangular mesas with $\ell/w = 20/3$ from the uniform *ac* Josephson current alone, when the mesa is suspended in vacuum. (a) At the fundamental $n = 1$ frequency with $k_1 w = \pi/n_r$. (b) At the second harmonic $n = 2$ with $k_2 w = 2\pi/n_r$.

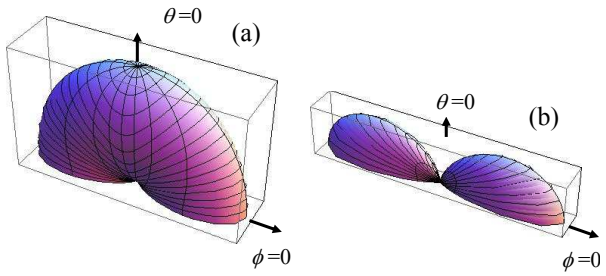

FIG. 14: (Color online) Three-dimensional plots of the radiation intensity in arbitrary units for rectangular mesas with $\ell/w = 20/3$ from the cavity source alone, when the mesa is suspended in vacuum. (a) The fundamental (10) cavity mode with $k_{10} w = \pi/n_r$. (b) The second harmonic (20) cavity mode with $k_{20} w = 2\pi/n_r$.

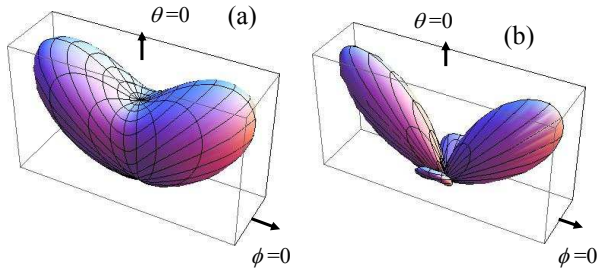

FIG. 15: (Color online) Plots of the intensity in arbitrary units for rectangular mesas with $\ell/w = 20/3$ of the combined radiation from Model I with $\alpha_1(0) = 0.2$ from the uniform *ac* Josephson current and the rectangular cavity modes when the mesa sits atop a superconducting substrate. (a) The fundamental $n = 1$ *ac* Josephson mode and the cavity (10) mode with $k_w = k_{10} w = \pi/n_r$. (b) The second harmonic with $k_2 w = k_{20} w = 2\pi/n_r$ and $\alpha_2(0) = 0.2$.

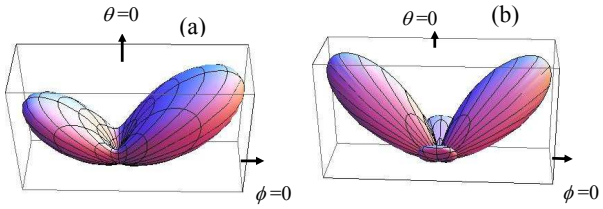

FIG. 16: (Color online) Plots of the intensity in arbitrary units for rectangular mesas with $\ell/w = 20/3$ of the coherently combined radiation when the mesa sits atop a superconducting substrate. (a) The fundamental $n = 1$ *ac* Josephson mode and the cavity (10) mode with $k_w = k_{10}w = \pi/n_r$, $x_1 = 0$ and $r_1 = 0.05$ (b) The second harmonic with $k_2 w = k_{20}w = 2\pi/n_r$, $x_2 = w/4$ and $r_2 = 0.6$.

superconducting substrates, both $S_n^J(\theta)$ and $\alpha_n(\theta)$ are proportional to $\cos\theta$, as shown in Sec. VI. The fraction of the radiation arising from the uniform *ac* Josephson current source at the fundamental frequency is then $[1 + (B_1'/A_1')\alpha_1(0)]^{-1}$, as was used in fits to experiments on rectangular mesas[21].

As for cylindrical mesas, the output from rectangular mesas is linearly polarized. Because the angular distribution of the output intensity at the fundamental frequency is very similar in both rectangular and cylindrical mesas, only minor differences in the angular distribution of the tilt angles for the two types of mesas are expected.

Let us now consider the case when the combination of the radiation sources is coherent. In this case, $dP_n/d\Omega$ of the nth harmonic is given by

$$\frac{dP_n}{d\Omega} \propto |S_n^J(\theta)|^2\Big(|-\sin\theta\chi_n + r_n(M_n^x\sin\phi - M_n^y\cos\phi)|^2 + |r_n|^2\cos^2\theta|M_n^x\cos\phi + M_n^y\sin\phi|^2\Big), \tag{32}$$

where $r_n = \tilde{E}_{0n}S_n^M(\theta)/[2\mu_0 J_n^J c S_n^J(\theta)]$. For $n = 1$, M_1^x and M_1^y, given in the Appendix, when evaluated at either $x_1 = 0$ or w are real, and a coherent combination is strongly asymmetric. For $n = 2$, however, both M_2^x and M_2^y are pure imaginary for $x_2 = \pm w/4$. Hence, the resulting coherent combination in $dP/d\Omega$ is the sum of that from the two sources. This is pictured in Fig. 16. In Fig. 16(a), the combined coherent output when $r_1 = 0.05$ is shown, computed when $x_1 = 0$. This figure shows a strong intensity asymmetry even for this small ratio of the outputs from the two sources, with the pattern exhibiting C_1 point group symmetry. In Fig. 16(b), the combined output for $n = 2$ is shown for the case $r_2 = 0.6$, computed with $x_2 = w/4$. In this case, the pattern has C_{2v} symmetry.

VIII. DISCUSSION AND SUMMARY

The first correct prescription of the incorporation of the Ampère boundary condition into the superconducting stack of Josephson junctions under the application of a *dc* voltage V_0, which itself generates THz radiation, was presented here. This prescription relied upon both of the Love equivalence principles. By the Love equivalence principle for a magnetic conductor, to calculate the radiation outside the mesa, the magnetic field inside the mesa generated by the *ac* Josephson current is effectively set equal to zero inside the cavity, and replaced by the equivalent surface electric current $\boldsymbol{J}_S$, which is the primary radiation source. Effectively setting $H_{||} = 0$ inside the mesa also sets the boundary condition for the cylindrical cavity. With this boundary condition, the cylindrical cavity modes are immediately found, and when the *ac* Josephson current effectively placed on the edge as $\boldsymbol{J}_S$ radiates at a frequency that matches one of the cavity modes, the inhomogeneous part of the *ac* Josephson current has a mode which resonates with a cavity mode of the same (or perhaps similar, in an extension of the model) spatial form, and the amplitude for that cavity mode then grows linearly in time, until it saturates, and then the cavity mode radiates in conjunction with the primary *ac* Josephson radiation at that frequency.

The form of the cavity radiation is obtained from Love's electric conductor equivalence principle, in which the equivalent of the cavity electric field is placed on the surface as a magnetic surface current density $\boldsymbol{M}_S$, which radiates in conjunction with the *ac* Josephson radiation equivalent electric surface current density $\boldsymbol{J}_S$. From the experiments on three cylindrical mesas, it is evident that the lowest energy cavity (11) mode has been excited. In addition, radiation at the second *ac* Josephson harmonic frequency was seen in all three cylindrical mesas[26]. Since the mismatch between these second harmonic frequencies and the nearest cavity mode frequency is 4%, about 5-6 standard deviations away from matching, this second harmonic radiation arises almost entirely from the primary radiation source, the *ac* Josephson radiation acting as a surface electric current density. In addition, the fact that the BSSCO mesa acts both as an electric conductor and as a magnetic conductor provides a mechanism to understand the role of a superconducting BSCCO substrate. Such substrates cause the emitted radiation to vanish along the direction parallel to it, greatly reducing the output power of the radiation.

While the main function of the inhomogeneous part of the *ac* Josephson current is that

it couples to a cavity mode, provided that the conditions are properly met, if the inhomogeneities are sufficiently strong, they can significantly alter the azimuthal and axial anisotropy of the combined radiation at the fundamental frequency, and especially that of the higher harmonics. In addition, it remains an open question as to whether the angular constants ϕ_{0n} are fixed or random during the time of the measurement. To the extent that the cylindrical cavity itself is perfectly homogeneous, one might expect no preferred angle for each mode of inhomogeneity. On the other hand, some feature involved in the experimental situation might lead to a fixed inhomogeneity direction. Only experiments measuring the angular distribution of the radiation and its polarization can distinguish these two situations. Although no figures to illustrate this point were displayed, if one were to assume the phase of the cavity mode for a fixed ϕ_{0n} could have either sign with equal probability, then the situation would be analogous to that of Model I for a rectangular mesa. For a cylindrical cavity, this model would preserve the point kink of the output radiation and restore C_{2v} point group symmetry, but the position of the kink would be at $\theta = 0°$, and the value of the output power would not vanish there.

For rectangular mesas, setting $H_{||} = 0$ on each of the edges leads to singularities in the analytic properties of the electromagnetic fields at the corners, greatly complicating the situation. Hence, most previous workers studied infinite strips, where the corners could be neglected. For the case of finite length rectangular mesas, the question of whether the combined radiation is skewed to one side of the mesa or the other is also relevant. If the mesa were symmetric, as in a cylinder with no preferred angle, one would average over the two configurations, resulting in a symmetric radiation pattern, and an incoherent combination of the radiation from the two sources, each of which is separately coherent. That was the purpose for the study of Models I and II.

Except in the calculation of the superconducting substrate factor, the cylindrical mesa was treated essentially as an infinitely thin disk, completely neglecting any spatial variation normal to the layers. While this is not a good approximation for treating heating inhomogeneities[22], it suffices for impurity inhomogeneities and the important lateral inhomogeneities in the *ac* Josephson current, which may be assumed to be the critical part of the microscopic mechanism that excites the cavity modes. Hence, exotic features such as inhomogeneous kinks along the z axis are omitted entirely, as they are completely unnecessary for the excitation of the cavity modes[27].

Cylindrical mesas are much simpler to understand theoretically than are rectangular mesas. There are several aspects to this simplicity. Most important, the von Neumann boundary condition is elementary in this geometry, whereas for a rectangle, it is treatable at the corners only by numerical techniques. In addition, the fact that none of the cylindrical cavity modes are harmonics of one another is an extremely important point, which is why cylindrical mesas were studied in the first place. Since rectangular cavities have higher energy modes that are also harmonics of a lower mode, such as the (10) or the (01) mode, the observation of harmonics in the output of rectangular mesas did not allow for a precise determination of the primary radiation source, which has now been clearly identified as the *ac* Josephson current, and not the cavity mode radiation. The primary role of the cavity mode is to lock the frequency of an *ac* Josephson mode (usually, if not always, the fundamental) onto that of a cavity mode, fixing ω_J to $\omega_{m_0 p_0}$ (evidently ω_{11}). Then, the displacement current arising from the laterally inhomogeneous *ac* Josephson current excites the $(m_0 p_0)$ cavity mode, allowing it also to radiate. From fits to experimental data on both rectangular and cylindrical cavities, it appears that at least half of the total output power arises from the primary source. The amplitudes relative to that of the fundamental of the higher harmonics are comparable to those in rectangular mesas, for which amplification by the excitation of higher cavity modes could occur[21]. Hence, such cavity mode amplification is rather weak.

The cavity modes of a cylindrical mesa are similar in form to those of a drum, and one or more of them can be amplified when a drummer strikes a particular region on the drum surface. The surface region of the drum struck does not need to have the precise shape of that of the main cylinder (drum) mode excited. By analogy, a modification of this theory of the cylindrical cavity mode amplification could occur without implementation of the von Neumann boundary condition, which provided a precise matching in spatial form of the cavity mode with that of the inhomogeneities. In a rectangular mesa, a subset of the cavity mode frequencies are harmonics of one another, and can be excited as by a player of a stringed instrument in lightly touching a finger at the midpoint or quarter point at either end of the string, for example, in order to make it sound one or two octaves higher than the fundamental, respectively.

This is the first treatment of the dramatic effect of superconducting substrates upon the output power of radiating BSCCO mesas. Using the same Love principle that was the

basis for the correct implementation of Ampère's law, the magnetic equivalence principle, it follows that superconducting substrates cause a drastic reduction in the output power of the radiation, especially for the power emitted near to $\theta = 90°$. Note that in predictions for the far-field intensity of both the primary *ac* Josephson current and the secondary cavity radiation sources, the intensity at the fundamental frequency and at $\theta = 90°$ is predicted to be at least comparable to that of its maximum output. The fact that in both rectangular and cylindrical mesas, the experimental intensity at $\theta = 90°$ is consistent with zero is a very strong indication that the perfect magnetic conductor model of superconducting substrates is correct. This model is also consistent with the experiments of Barbara *et al.*, in which the output of a conventional Josephson junction array with the currents parallel to the superconducting substrate was enhanced by the substrate (or ground plane) prior to its entry into the waveguide[33–35]. Hence, removal of the superconducting substrate from BSCCO mesas could enhance the output by at least two orders of magnitude, and by replacing the substrate with a perfect electric conductor such as Cu, one could further enhance the output by a factor of four. This could allow for output as high as 5mW, which would be more than sufficient for many practical applications.

In summary, the primary microscopic source of the coherent radiation from the intrinsic Josephson junctions in mesas of BSCCO has been identified as the non-linear *ac* Josephson current. Its uniform part acts as an electric current density source and its non-uniform part excites one of the linear cavity modes, which sets the wavelength of the fundamental *ac* Josephson frequency to the appropriate sample dimension and acts as a magnetic surface current density source. The two sources radiate together at the fundamental *ac* Josephson frequency. For rectangular mesas, such matching can also occur for higher harmonics, but for cylindrical mesas, only one of the harmonic frequencies present in the *ac* Josephson current can be amplified by the linear electromagnetic cavity. The combination of these two coherent sources can be either coherent or incoherent. It suffices to treat all of the junctions as acting in unison. For radiation at the fundamental *ac* Josephson frequency locked onto the cylindrical cavity (11) mode, the combined output radiation pattern has a linear electric field polarization that is usually but not always along $\hat{\boldsymbol{\theta}}$. Radiation at the second harmonic frequency in cylindrical mesas arises almost exclusively from the *ac* Josephson current, is also linearly polarized, and is purely coherent. The output from rectangular mesas should also be linearly polarized. It is emphatically noted that removal of the superconducting

substrate, or better yet, replacement of it by a perfect electric conductor such as Au or Cu, could lead to an enhancement of the output power of the mesas from the highest observed power of 5μ W up to 5 mW, suitable for many applications. An appropriate name for this device is Josephson STAR emitter, for Josephson stimulated terahertz amplified radiation emitter.

ACKNOWLEDGMENTS

We thank X. Hu, S. Lin, B. Markovic, N. F. Pedersen, and M. Tachiki for stimulating discussions. This work was supported in part both by the JST (Japan Science and Technology Agency) CREST project, by the WPI Center for Materials Nanoarchitechtonics (MANA), by the JSPS (Japan Society for the Promotion of Science) CTC program and by the Grant-in Aid for Scientific Research (A) under the Ministry of Education, Culture, Sports, Science and Technology (MEXT) of Japan. One of us (R.A.K.) would also like to thank the University of Tsukuba for its kind hospitality.

APPENDIX

A. Spatial fluctuations of the *ac* Josephson current

If the *ac* Josephson current were spatially uniform within the mesa, it could only couple to a uniform electric field, which cannot radiate. Hence, the non-uniform part $\delta J_n(\boldsymbol{x}')$ of the *ac* Josephson current must provide the coupling to the electric field. There may be a number of sources for this non-uniformity, such as defects and thermal fluctuations, which may be enhanced by inhomogeneous heating effects[22]. Here it is assumed that the primary source of the inhomogeneities is thermodynamic fluctuations, but the model can also be employed to approximate smooth stoichiometry variations[29, 30]. In the samples used in the experiments[26], the BSCCO crystals were prepared slowly over a very limited central region in gold-plated elliptical heating ovens, with highly controlled heating, producing samples that are probably much more uniform chemically (although still highly non-stoichiometric) than in those studies[31, 32].

Assuming $[\langle(\delta J_n)^2\rangle]^{1/2} \ll J_n^J$, the Helmholtz free energy of these fluctuations may be

written as

$$\mathcal{F}_f \propto \sum_{n=1}^{\infty} \int d^2\boldsymbol{r}'[(\delta J_n)^2 + (\xi_n')^2(\boldsymbol{\nabla}'\delta J_n)^2], \tag{33}$$

where $\xi_n'(T)$ is a temperature-dependent characteristic length over which the spatial fluctuations in δJ_n occur, and n describes the intralayer spatial variations associated with the nth harmonic of the ac Josephson frequency, as presented in Eq. (7). $\mathcal{F}_f$ is a minimum when

$$-(\xi_n')^2(\boldsymbol{\nabla}')^2\delta J_n + \delta J_n = 0, \tag{34}$$

which is written in cylindrical coordinates. The full solution to this equation may be written as

$$\delta J_n(\rho', \phi') = \sum_{m=0}^{\infty} C_m^{(n)} J_m(\rho'/\xi_n') \cos[m(\phi' - \phi_{0n})], \tag{35}$$

where the ϕ_{0n} and $C_m^{(n)}$ are free parameters and the general m dependence of ϕ_{0n} is neglected for simplicity[5]. The ac Josephson current vanishes outside the mesa ($\rho' > a$), but since its uniform part J_n^J is discontinuous with a vanishing derivative at the mesa edge, δJ_n may also be discontinuous at $\rho' = a$. Here it is assumed that thermodynamic fluctuations are weak near the mesa edge, so that one may take

$$\frac{\partial \delta J_n}{\partial \rho'}\Big|_{\rho'=a} = 0. \tag{36}$$

With this von Neumann boundary condition, $\delta J_n(\boldsymbol{x}')$ may be written as

$$\delta J_n(\boldsymbol{x}') = \sum_{p=1,m=0}^{\infty} C_{mp}^{(n)} J_m(k_{mp}'\rho') \cos[m(\phi' - \phi_{0n})], \tag{37}$$

where $\chi_{mp} = k_{mp}'a$ is the pth non-vanishing value of $dJ_m(x)/dx = 0$, and $k_{mp}' = 1/\xi_{mp}'$. The χ_{mp} values for $m = 0, \ldots, 10$ and $p = 1, \ldots, 6$ are given in Table I. Since $\int_0^a \rho' d\rho' J_0(k_{0p}'\rho') = (a/k_{0p}')J_1(k_{0p}'a) = 0$ for $p \geq 1$, the spatial average of $\delta J_n(\boldsymbol{x}')$ vanishes, as required. Note that k_{mp}' represents the set of $1/\xi_n'$ values that satisfy the assumed boundary condition. In addition, since J_n^J and $\delta J_n(\boldsymbol{x}')$ are real, all of the $C_{mp}^{(n)}$ are real.

B. Excitation of a cavity mode

Let us next consider the cavity model of a very thin cylindrical mesa. The magnetic vector potential $\boldsymbol{A}(\boldsymbol{x}', t) = A_z(\boldsymbol{x}', t)\hat{\boldsymbol{z}}'$ satisfies

$$\boldsymbol{\nabla}'^2 A_z - \mu\epsilon\frac{\partial^2 A_z}{\partial t^2} = -\mu J_z(\boldsymbol{x}', t) \tag{38}$$

inside the mesa, where μ and ϵ are the magnetic permeability and dielectric constant inside it, $n_r = \sqrt{\mu\epsilon} \approx \sqrt{\epsilon}$, and $\boldsymbol{J}(\boldsymbol{x}', t) = \hat{\boldsymbol{z}}' J_z(\boldsymbol{x}', t)$ is given by the spatially inhomogeneous part of Eq. (7). As part of Love's magnetic equivalence principle, Eq. (38) is subject to the condition $-\frac{\partial A_z}{\mu \partial \rho'}\Big|_{\rho'=a} = H_\phi\Big|_{\rho'=a} = 0$, and the spatially uniform part of $\boldsymbol{J}(\boldsymbol{x}', t)$ cannot excite any cavity modes, but should be placed on the surface as a surface electric current density $\boldsymbol{J}_S$ from the Ampère boundary condition[3, 4], as in Sec. II. Hence, this boundary condition is precise, unlike the assumption made for $\delta J_n(\boldsymbol{x}')$. This boundary condition then leads to the same set of discrete wave vector amplitudes $k'_{mp} = \chi_{mp}/a$ as were assumed to be present in $\delta J_n(\boldsymbol{x}')$. Hence,

$$\boldsymbol{\nabla}'^2 A_z - \mu\epsilon \frac{\partial^2 A_z}{\partial t^2} \;=\; -\mu \sum_{m=0;p,n=1}^{\infty} e^{-in\omega_J t} C_{mp}^{(n)} J_m(k'_{mp}\rho') \cos[m(\phi' - \phi_{0n})], \tag{39}$$

which is satisfied by the particular solution

$$\begin{aligned} A_z^{(p)}(\boldsymbol{x}', t) \;=\; & \sum_{m=0;n,p=1}^{\infty} e^{-in\omega_J t} [A_{mp}^{(n)}(t)\delta_{m,m_0}\delta_{p,p_0} \\ & + A_{mp}^{(n)}(1 - \delta_{m,m_0}\delta_{p,p_0})] J_m(k'_{mp}\rho') \cos[m(\phi' - \phi_{0n})], \end{aligned} \tag{40}$$

provided that

$$A_{m_0p_0}^{(n)}(t) \;=\; t\frac{iC_{m_0p_0}^{(n)}}{2n\epsilon\omega_J} \qquad \text{for } (mp) = (m_0p_0), \tag{41}$$

$$\omega_{m_0p_0}^2 \;=\; n^2\omega_J^2 \qquad \text{for } (mp) = (m_0p_0), \tag{42}$$

$$A_{mp}^{(n)} \;=\; \frac{C_{mp}^{(n)}}{\epsilon(\omega_{mp}^2 - n^2\omega_J^2)} \text{ for } (mp) \neq (m_0p_0), \tag{43}$$

where $k'_{m_0p_0} = \omega_{m_0p_0} n_r/c$. Although Eq. (41) could apply to general (mp), Eq. (42) can at most apply to a single value of (mp), which is denoted (m_0p_0). The other modes are far from resonance with negligible amplitudes and Lorentzian lineshapes as suggested by Eq. (43). Of course, effects such as a built-in z-dependence to the cylinder radius a during mesa fabrication will give finite widths $\propto 1/Q_{mp}$ to the cavity modes.

Note that the t in the solution for the excited (m_0p_0) mode causes the amplitude $A_{m_0p_0}^{(n)}(t)$ of that mode to grow linearly in time, which continues until saturation is achieved, and radiation occurs. During radiation, the amplitude of the resonant frequency is approximately constant in time, which may be taken to have the finite value $A_{m_0p_0}^{(n)}(\infty) \equiv \lim_{t\to\infty} A_{m_0p_0}^{(n)}(t)$. From Eq. (41), the resonant amplitude $A_{m_0p_0}^{(n)}(t)$ for small t is purely imaginary for a real ϵ

in the frequency range of interest, so it may be assumed that it stays purely imaginary after saturation, and one may write

$$A^{(n)}_{m_0p_0}(\infty) \;=\; it_{\rm eff}\frac{C^{(n)}_{m_0p_0}}{2n\epsilon\omega_J}, \tag{44}$$

where $t_{\rm eff}$ is the effective time to reach saturation.

D. Resonant cavity radiation

The electric vector potential $\boldsymbol{F}_{\rm r}$ resulting from the resonant cavity mode in the radiation zone is

$$\begin{aligned}\boldsymbol{F}_{\rm r}(\boldsymbol{x},t) \;\underset{r/a\gg1}{\rightarrow}\; & \frac{iv\epsilon_0}{4\pi r}\omega_{mp}A^{(n)}_{mp}(\infty)S^M_{mp}(\theta)e^{i(k_{mp}r-\omega_{mp}t)} \\ & \times J_m(k'_{mp}a)\int_0^{2\pi}\frac{d\phi'}{2\pi}\hat{\boldsymbol{\phi}}'\cos[m(\phi'-\phi_{0n})]e^{-ik_{mp}a\sin\theta\cos(\phi-\phi')}\Big|_{\substack{p=p_0\\m=m_0}},\end{aligned} \tag{45}$$

where $\omega_{m_0p_0}=n\omega_J$ and $k_{m_0p_0}=\omega_{m_0p_0}/c$ outside the mesa, and $S^M_{mp}(\theta)=1$ when the mesa is suspended in vacuum. After setting $\hat{\boldsymbol{\phi}}'=\hat{\boldsymbol{\theta}}\cos\theta\sin(\phi-\phi')+\hat{\boldsymbol{\phi}}\cos(\phi-\phi')$, and evaluating the integral over ϕ', one obtains

$$\begin{aligned}\boldsymbol{F}_{\rm r}(\boldsymbol{x},t) \;\underset{r/a\gg1}{\rightarrow}\; & -(-i)^{m-1}\frac{G^{(n)}_{mp}\epsilon_0}{k_{mp}}\frac{e^{i(k_{mp}r-\omega_{mp}t)}}{4\pi r} \\ & \times\Big[\hat{\boldsymbol{\theta}}\cos\theta\sin[m(\phi-\phi_{0n})]J^+_m(k^\theta_{mp})-\hat{\boldsymbol{\phi}}\cos[m(\phi-\phi_{0n})]J^-_m(k^\theta_{mp})\Big]\Big|_{\substack{p=p_0\\m=m_0}}\end{aligned} \tag{46}$$

where $G^{(n)}_{mp}$ is given by Eq. (17), $k^\theta_{mp}=k_{mp}a\sin\theta$, and $J^\pm_m(z)=[J_{m+1}(z)\pm J_{m-1}(z)]/2$. It is then straightforward to obtain $\boldsymbol{E}_{\boldsymbol{F}_{\rm r}}(\boldsymbol{x},t)$, which is given by Eq. (16).

D. Vector potentials and surface currents for rectangular mesas

For the rectangular mesas studied in Sec. VII, $\boldsymbol{A}(\boldsymbol{x},t)$ and $\boldsymbol{F}(\boldsymbol{x},t)$ in spherical coordinates are given in the radiation zone by

$$\boldsymbol{A}(\boldsymbol{x},t) \;\rightarrow\; \frac{\mu_0\hat{\boldsymbol{z}}\tilde{v}}{8\pi r}\sum_{n=1}^{\infty}J^J_n e^{in(k_Jr-\omega_Jt)}S^J_n(\theta)\chi_n, \tag{47}$$

$$\chi_n(\theta,\phi) \;=\; \cos X_n\frac{\sin Y_n}{Y_n}+\cos Y_n\frac{\sin X_n}{X_n}, \tag{48}$$

$$\boldsymbol{F}(\boldsymbol{x},t) \;\rightarrow\; -\frac{\epsilon_0\tilde{v}}{16\pi r}\sum_{n=1}^{\infty}\tilde{E}_{0n}e^{in(k_Jr-\omega_Jt)}S^M_n(\theta)(\hat{\boldsymbol{x}}M^x_n+\hat{\boldsymbol{y}}M^y_n), \tag{49}$$

$$M_n^x = -\sin Y_n \sum_{\sigma=\pm} \sigma e^{i\sigma n\pi x_n/w} \frac{\sin(X_{n,\sigma})}{X_{n,\sigma}}, \tag{50}$$

$$M_n^y = \frac{\sin Y_n}{Y_n} \sum_{\sigma=\pm} e^{i\sigma X_n} \sin\Big(\frac{n\pi}{2} + \frac{\sigma n\pi x_n}{w}\Big), \tag{51}$$

where $X_n = (k_n w/2)\sin\theta\cos\phi$, $Y_n = (k_n \ell/2)\sin\theta\sin\phi$, $k_n w = n\pi/n_r$, $X_{n,\sigma} = n\pi/2 + \sigma X_n$, $\tilde{v} = w\ell h$, $S_n^M(\theta) = S_n^J(\theta) = 1$ for no substrate, $\hat{\boldsymbol{x}} = \hat{\boldsymbol{r}}\sin\theta\cos\phi + \hat{\boldsymbol{\theta}}\cos\theta\cos\phi - \hat{\boldsymbol{\phi}}\sin\phi$, $\hat{\boldsymbol{y}} = \hat{\boldsymbol{r}}\sin\theta\sin\phi + \hat{\boldsymbol{\theta}}\cos\theta\sin\phi + \hat{\boldsymbol{\phi}}\cos\phi$, and x_n appears in Eq. (28).

The quantities present in the expression for the output power intensity from the combined electric and magnetic surface current density sources follow. For the portion of the output power resulting from the uniform portion of $\boldsymbol{J}_S$, Eqs. (47) and (48) are sufficient. The part of the combined output arising from $\boldsymbol{M}_S$ is more complicated, and the combination can be either coherent or incoherent, as for the output from cylindrical mesas. When the combination is coherent, we assume that $H_y(x' = \pm w/2) = 0$ is maintained along both lengths of the mesa, but the output power $P(x_n)$ is evaluated when x_n is either 0 or w/n for n odd, or when $x_n = \pm w/2n$ for n even. When the output from the two sources is incoherent with respect to one another, one may average $P(x_n)$ in two models. In Model I, it is assumed that $H_y(x' = \pm w/2) = 0$ is maintained along both lengths of the mesa, so that $\langle P(x_n)\rangle_I = \frac{1}{2}[P(0)+P(w/n)]$ for n odd, and $\langle P(x_n)\rangle_I = \frac{1}{2}[P(w/2n)+P(-w/2n)]$ for n even. In Model II, the boundary condition upon H_y is relaxed, and one averages $P(x,n)$ over all x_n values that preserve the wave vector within the mesa, $\langle P(x_n)\rangle_{II} = (n/2w)\int_{-w/n}^{w/n} P(x_n)dx_n$. In both models, the average output power is characterized by three functions $C_n^i(\theta,\phi)$, $D_n^i(\theta,\phi)$, and $E_n^i(\theta,\phi)$ for $i =$ I and II. For Model I, $C_n^I = A_n^2$, $D_n^I = B_n^2$, and $E_n^I = 2A_nB_n$, where for n either odd or even,

$$A_n = \sin Y_n \sum_{\sigma=\pm} \frac{\sigma^n \sin(X_{n,\sigma})}{X_{n,\sigma}}, \tag{52}$$

$$B_n = 2\frac{\sin Y_n}{Y_n} \sin\Big(\frac{n\pi}{2} + X_n\Big). \tag{53}$$

For Model II,

$$C_n^{II} = \sin^2 Y_n \sum_{\sigma=\pm} \Big(\frac{\sin(X_{n,\sigma})}{X_{n,\sigma}}\Big)^2, \tag{54}$$

$$D_n^{II} = \frac{\sin^2 Y_n}{Y_n^2}\Big(1 - (-1)^n\cos(2X_n)\Big), \tag{55}$$

$$E_n^{II} = 2\frac{\sin^2 Y_n}{Y_n} \sum_{\sigma=\pm} \frac{\sigma\sin^2(X_{n,\sigma})}{X_{n,\sigma}}, \tag{56}$$

where X_n, Y_n, and $X_{n,\sigma}$ are given following Eq. (51).

---

* Electronic address: klemm@physics.ucf.edu

† Electronic address: kadowaki@ims.tsukuba.ac.jp

[1] L. Ozyuzer, A. E. Koshelev, C. Kurter, N. Gopalsami, Q. Li, M. Tachiki, K. Kadowaki, T. Yamamoto, H. Minami, H. Yamaguchi, T. Tachiki, K. E. Gray, W.-K. Kwok, and U. Welp, Science **318**, 1291 (2007).

[2] K. Kadowaki, H. Yamaguchi, K. Kawamata, T. Yamamoto, H. Minami, I. Kakeya, U. Welp, L. Ozyuzer, A. Koshelev, C. Kurter, K. E. Gray, and W.-K. Kwok, Physica C **468**, 634 (2008).

[3] C. A. Balanis, *Antenna Theory, Analysis and Design*, (Wiley, Hoboken, NJ, third edition, 2005).

[4] C. A. Balanis, *Advanced Engineering Electromagnetics*, (Wiley, Hoboken, NJ, 1989).

[5] J. D. Jackson, *Classical Electrodynamics*, (Wiley, NY, third edition, 1999).

[6] L. N. Bulaevskii and A. E. Koshelev, J. Supercond. and Novel Magn. **19**, 349 (2006).

[7] L. N. Bulaevskii and A. E. Koshelev, Phys. Rev. Lett. **99**, 057002 (2007).

[8] A. E. Koshelev, Phys. Rev. B **78**, 174509 (2008).

[9] S. Lin and X. Hu, Phys. Rev. Lett. **100**, 247006 (2008).

[10] S. Lin and X. Hu, Phys. Rev. B **79**, 104507 (2009).

[11] S. Lin and X. Hu, ArXiv:0903.5510 (unpublished).

[12] S. Lin and X. Hu, J. Supercond. Nov. Magn. (to be published) (ArXiv:0905.2486).

[13] X. Hu and S. Lin, Phys. Rev. B **78**, 134510 (2008).

[14] X. Hu and S. Lin, Phys. Rev. B **80**, 064516 (2009).

[15] H. Matsumoto, T. Koyama, and M. Machida, Physica C **468**, 654 (2008).

[16] H. Matsumoto, T. Koyama, M. Machida, and M. Tachiki, Physica C **468**, 1899 (2008).

[17] S. Lin, X. Hu, and M. Tachiki, Phys. Rev. B **77**, 014507 (2008).

[18] M. Tachiki, S. Fukuya, and T. Koyama, Phys. Rev. Lett. **102**, 127002 (2009).

[19] M. Tachiki, T. Koyama, and S. Fukuya, ArXiv:0907.1770 (unpublished).

[20] T. Koyama, H. Matsumoto, M. Machida, and K. Kadowaki, Phys. Rev. B **79**, 104522 (2009).

[21] K. Kadowaki, M. Tsujimoto, K. Yamaki, T. Yamamoto, T. Kashiwagi, H. Minami, M. Tachiki, and R. A. Klemm, J. Phys. Soc. Jpn. **79**, 023703 (2010).

[22] H. B. Wang, S. Guénon, J. Yuan, A. Iishi, S. Arisawa, T. Hatano, T. Yamashita, D. Koelle, and R. Kleiner, Phys. Rev. Lett. **102**, 017006 (2009).

[23] R. A. Klemm and K. Kadowaki, J. Supercond. Nov. Magn. **23**, 613 (2010).

[24] S. A. Schelkunoff, Bell Syst. Tech. J. **15**, 92 (1936).

[25] A. E. H. Love, Phil. Trans. Roy. Soc. London, Ser. A **197**, 1 (1901).

[26] M. Tsujimoto, K. Yamaki, T. Yamamoto, T. Kashiwagi, H. Minami, M. Tachiki, K. Kadowaki, and R. A. Klemm, (unpublished).

[27] Hu and Lin in their Fig. 6 also found results of the radiation patterns from the cylindrical cavity (11), (12), (01), and (21) modes[14]. Although their paper described numerical calculations inside the mesa, their results essentially agree with those shown in Figs. (4) and (5) for the radiation-zone output power emanating from the cavity modes alone from a sample suspended in vacuum. They also used the same boundary condition as employed here for the cavity excitations, $H_\phi = 0$, but they did not include the electric surface current $\boldsymbol{J}_S$, violating Love's magnetic equivalence principle[3, 4]. They also made no mention of the superconducting substrate, and did not predict any higher harmonics to be observable, so their results are in qualitative disagreement with experiment[26].

[28] R. A. Klemm, A. Luther, and M. R. Beasley, Phys. Rev. B **12**, 877 (1975).

[29] H. Eisaki, N. Kaneko, D. L. Feng, A. Damascelli, P. K. Mang, K. M. Shen, Z.-X. Shen, and M. Greven, Phys. Rev. B **69**, 064512 (2004), and many references within.

[30] D. Grebille, H. Leligny, A. Ruyter, P. Labbé, and B. Raveau, Act. Cryst. B **52**, 628 (1996).

[31] T. Mochiku and K. Kadowaki, Physica C **235-240**, 523 (1994).

[32] T. Mochiku, K. Hirata and K. Kadowaki, Physica C **282-287**, 475 (1997).

[33] P. Barbara, A. B. Cawthorne, S. V. Shitov, and C. J. Lobb, Phys. Rev. Lett. **82**, 1963 (1999).

[34] P. Barbara, A. B. Cawthorne, S. V. Shitov, and C. J. Lobb, Phys. Rev. B **60**, 7575 (1999).

[35] B. Vasilič, S. V. Shitov, C. J. Lobb, and P. Barbara, Appl. Phys. Lett. **78**, 1137 (2001).